PAPER

Check for updates

Silk fibroin photo-lyogels containing microchannels as a biomaterial platform for *in situ* tissue engineering†

Marissa Baptista,[a] Habib Joukhdar,[a] Cesar R. Alcala-Orozco, [b] Kieran Lau,[a] Shouyuan Jiang,[a] Xiaolin Cui, [b,c] Steven He,[a] Fengying Tang,[a,d] Celine Heu,[e] Tim B. F. Woodfield, [b,c,f] Khoon S. Lim [*b,c,f] and Jelena Rnjak-Kovacina [*a]

The biophysical properties of biomaterials are key to directing the biological responses and biomaterial integration and function in *in situ* tissue engineering approaches. We present silk photo-lyogels, a biomaterial format fabricated using a new combinatorial approach involving photo-initiated crosslinking of silk fibroin *via* di-tyrosine bonds followed by lyophilization to generate 3D, porous lyogels showing physical properties distinct to those of lyophilized silk sponges or silk hydrogels. This fabrication approach allowed introduction of microchannels into 3D constructs *via* biofabrication approaches involving silk crosslinking around an array of 3D printed photocurable resin pillars to generate parallel channels or around a 3D printed sacrificial thermosensitive gel to generate interconnected channels in a rapid manner and without the need for chemical modification of silk fibroin. The presence of interconnected microchannels significantly improved migration of endothelial cells into 3D photo-lyogels *in vitro*, and tissue infiltration, photo-lyogel integration, and vascularization when implanted *in vivo* in a mouse subcutaneous model. Taken together, these findings demonstrate the feasibility and utility of a new combinatorial fabrication approach for generation of silk biomaterials that support cell interactions and implant integration for *in situ* tissue engineering approaches.

1. Introduction

Biomaterials play a key role in tissue engineering and regenerative medicine approaches toward replacement and regeneration of missing or injured tissues. Biochemical and biophysical properties of biomaterials are key drivers of their biological interactions and performance, and this is particularly true for *in situ* tissue engineering approaches.[1] *In situ* tissue engineering is biomaterial-driven endogenous regeneration occurring directly at the site of injury, as opposed to traditional tissue engineering which involves tissue culture and maturation *in vitro*.[1,2] The advantages of this approach include reduced cost, time, and regulatory hurdles associated with traditional *in vitro* tissue engineering, with off-the-shelf biomaterials implanted directly at the site of injury and over time transformed into autologous tissue.[1] Biomaterial features including chemical, mechanical, morphological, and degradation properties play a key role in driving biological interactions in the body, with the biomaterial acting as a temporary instructive environment that endogenous cells interact with to create new tissue.[1,3] Architectural cues provided by the pore morphology of certain biomaterials have been demonstrate to influence a number of key biological processes involved in tissue regeneration, including cell infiltration, tissue vascularization, macrophage polarization, and the foreign body response.[3] Additionally, vessel-like microchannel structures introduced into biomaterials have been demonstrated to play a major role in biomaterial interactions with the native tissue, influencing tissue infiltration, vascular ingrowth, and tissue remodeling in the body.[4]

Silk fibroin has become increasingly popular as a biomaterial toward a range of tissue engineering applications due to its

[a] *Graduate School of Biomedical Engineering, University of New South Wales, Sydney, NSW, Australia. E-mail: j.rnjak-kovacina@unsw.edu.au*
[b] *Christchurch Regenerative Medicine and Tissue Engineering (CReaTE) group, Department of Orthopaedics Surgery and Musculoskeletal Medicine, University of Otago, Christchurch, 8011, New Zealand. E-mail: khoon.lim@otago.ac.nz*
[c] *Medical Technologies Centre of Research Excellence, New Zealand*
[d] *Currently at Comparative Pathology Program, Department of Comparative Medicine, University of Washington School of Medicine, Seattle, Washington, USA*
[e] *Biomedical Imaging Facility, University of New South Wales, Sydney, NSW 2052, Australia*
[f] *Maurice Wilkins Centre for Molecular Biodiscovery, New Zealand*
†Electronic supplementary information (ESI) available. See DOI: 10.1039/d0bm01010c

favorable biological properties and ease of processing into diverse material formats offering a great degree of control over its physical and biological features,[5] making it a particularly promising material toward *in situ* tissue engineering approaches. One of the distinguishing features of silk fibroin is the ability to crosslink the protein in aqueous environments *via* induction of beta-sheet formation in the absence of chemical crosslinkers.[6] Control over the degree of beta-sheet formation has been optimized *via* a range of techniques and has become a powerful means of fine tuning the mechanical and degradation properties of silk biomaterials.[7,8] However, hydrogels made *via* beta-sheet formation tend to be brittle, difficult to handle and slow degrading, limiting cellular remodeling and applications in soft tissue engineering.[9] More recently, silk hydrogels crosslinked *via* formation of di-tyrosine bonds have gained considerable attention in the biomaterials field due to their elastomeric nature and favorable biological interactions.[9–11] This approach utilizes the relatively high degree of tyrosine residues in silk fibroin to form di-tyrosine crosslinks using a variety of radical-based chemical, enzymatic, or photo-initiated crosslinking approaches.[12]

Hydrogels are a popular biomaterial format due to their highly hydrated nature mimicking the native extracellular matrix, ability to encapsulate cells, and the ability to perform crosslinking directly at the site of injury.[13] However, the nanoscale mesh size of hydrogels limits *in situ* tissue ingrowth and vascularization and restricts the range of cues that can be engineered into hydrogel biomaterials for *in situ* tissue engineering approaches.[13] Lyogels (or related cryogels), or ice-templated hydrogels, on the other hand preserve many of the advantageous features of hydrogels, including their highly hydrated nature, while allowing introduction of microscale pores in a tunable manner. Additionally, the more rigid nature of lyogels facilitates sample handling and implantation, compared to hydrogels,[14] while the dry state allows storage and off-the-shelf use. Lyogels are fabricated by freezing and lyophilization of crosslinked hydrogel networks, where the control over ice crystal size and shape dictates the pore morphology. For example, unidirectional freezing allows formation of aligned, elongated ice crystals that when removed result in aligned pores that can facilitate cell and tissue alignment following implantation.[15,16] A few reports of silk based lyogels have been published and it has been demonstrated that the crosslinked nature of the starting protein network results in unique physicochemical properties compared to lyophilized sponges made by lyophilizing uncrosslinked silk solution.[14,16–19] While lyophilized silk sponges have been widely explored and evaluated for applications such as soft tissue,[20–22] intervertebral disc,[23] and cardiovascular tissue[24–26] augmentation and regeneration, platelet production,[27] and drug delivery,[28,29] silk lyogels are less well characterized. In particular, the properties of silk lyogels made from di-tyrosine crosslinked silk networks have not been explored to date. The nature and degree of crosslinking play a role in the final material properties,[18] demonstrating the importance of understanding the effect of processing parameters in lyogel formation.

In this work, we describe the physical and biological properties of silk lyogels made from silk hydrogels crosslinked using photo-initiated di-tyrosine crosslinking (photo-lyogels) as a potential biomaterial for *in situ* tissue engineering. We describe biofabrication methods for introducing arrays of parallel or interconnected microchannels through the scaffold toward promoting improved cell and tissue infiltration and construct integration *in vivo*. Microchannels are a well-established architectural feature that is commonly introduced into 3D biomaterials to promote mass transfer, cell migration, and tissue and blood vessel infiltration.[4] This combinatorial approach to silk lyogel formation has not been explored to date and offers key benefits in material fabrication, including ease and speed of processing allowing formation of intricate microchannel structures in porous 3D biomaterials in the absence of silk protein modification, and distinct physical and mechanical features.

2.   Materials and methods

Bombyx mori silk cocoons were obtained from Tajima Shoji Co Ltd (Japan). Female C57BL/6 mice were sourced from Australian Bio Resources (Australia). Human umbilical cord endothelial cells (HUVEC) were sourced from Lonza (Australia). All other reagents were purchased from Sigma-Aldrich unless stated otherwise.

2.1   Silk fibroin isolation

Silk fibroin (referred to as silk throughout) solution was prepared as previously described.[6] Briefly, *Bombyx mori* silk cocoons were cut into 2 cm² pieces and boiled in 0.02 M sodium carbonate solution (2.5 g fibers per L sodium carbonate) for 30 min to remove sericin. Silk fibroin fibers were washed in water and dissolved in 9.3 M lithium bromide (4 ml g⁻¹ silk fibers) for 4 h at 60 °C. The solution was dialyzed against water using SnakeSkin™ dialysis tubing (3500 MWCO, Thermo Fisher Scientific, USA) for 3 days. The concentration of the silk solution (6–8% wt/v) was determined by drying a known volume and weighing the remaining film. Silk solution was stored at 4 °C.

2.2   Silk photo-lyogel fabrication

All photo-lyogels were produced by photo-crosslinking a 4% (wt/v) silk solution in specialized molds, followed by freezing at −20 °C and lyophilization. Silk was crosslinked *via* di-tyrosine bond formation as previously described.[11] Briefly, silk solution was mixed with tris(2,2′-bipyridyl)dichlororuthenium (II) hexahydrate (Ru) and sodium persulfate (SPS) to a final concentration of 0.5 mM Ru and 5 mM SPS and irradiated with 30 mW cm⁻² light between 400 and 450 nm for 3 minutes. Silk photo-lyogels without microchannels (NC) were cast in flat 15 × 15 × 2 mm 3D printed molds (SLA photo-crosslinkable resin, Form2 SLA printer, Formlabs, USA), while photo-lyogels with parallel channels (PC) were cast in the same molds but with vertical pillars (500 μm dimeter and 1 mm

spacing between the pillars). Following lyophilization, photo-lyogels were removed from the molds, leaving an array of vertical parallel channels spanning the scaffolds. Photo-lyogels with interconnected channels (IC) were fabricated by casting the silk solution around a 3D printed sacrificial scaffold made from Pluronic® F-127. The sacrificial scaffold was printed using a BioScaffolder (SYS + ENG, Germany) from 30% (wt/v) Pluronic® F-127 (500 μm diameter struts, 1 mm spacing between the struts, 0–90° repeating pattern). The sacrificial polymer was removed by dissolution in water at 4 °C prior to lyophilization, leaving behind an interconnected network of microchannels. All photo-lyogels were hydrated in water or PBS and trimmed to 4 mm diameter and 2 mm height prior to use.

2.3 Characterization of silk photo-lyogel morphology

The morphology of silk photo-lyogels was assessed by scanning electron microscopy (SEM) and confocal microscopy. For scanning electron microscopy preparation, silk photo-lyogels ($n > 2$) were not hydrated and instead were mounted onto the 12.5 mm SEM stubs with carbon tape. To ensure adhesion and conductivity, silver dag was applied to the base of the photo-lyogel and allowed to dry overnight. The mounted samples were then gold sputter coated and imaged on a Hitachi S3400 SEM, with a 10 kV electron beam. Images were taken of each quadrant of photo-lyogel, and additionally all channels were imaged. To quantify pore size a 10 000 μm² grid was overlaid on each image and pores which fell at the intersection of each grid junction were measured for area using the ImageJ free-form selection tool. Pore morphology was measured as pore inlet area/pore size (μm²) and pore circularity and expressed as mean ± standard error of the mean. All the channels in a given sample were measured using ImageJ freeform selection tool to quantify channel inlet cross sectional area and circularity. For confocal imaging samples ($n = 2$) hydrated in water were incubated in 50 μg mL⁻¹ tetramethylrhodamine isothiocyanate mixed isomers (TRITC) (Life Technologies) for 2 hours and imaged on a Leica TCS SP2 Confocal Microscope with a 10× objective and a 561 nm laser. 200 μm thick z-stacks were collected with step size of 4–6 μm.

2.4 Silk photo-lyogel swelling and degradation

Silk photo-lyogels ($n = 8$) were washed thoroughly in water, then hydrated in water overnight and weighed the following day. Samples were blotted lightly on a tissue and rehydrated in PBS overnight to be weighed again the next day. Lastly, samples were dried overnight at 60 °C and weighed a final time. Swelling was determined by calculating the swelling ratio as $(W_r - W_d)/W_d$, where W_r is the mass of the rehydrated cryogel and W_d is the mass of the dry cryogel.[14]

To measure the relative degradation rates, photo-lyogels were weighed and then incubated in protease XIV (2 U mL⁻¹ in PBS) ($n = 5$) or PBS ($n = 3$) at 37 °C. At each time point, the protease solution or PBS was removed, and photo-lyogels were washed with water and dried at 60 °C overnight. Dry photo-lyogels were then weighed, placed in fresh protease or PBS and

the whole process was repeated. Degradation was calculated as percent weight change.

2.5 Mechanical properties of silk photo-lyogels

Bulk Young's modulus of silk photo-lyogels ($n = 4$) hydrated in PBS, was measured using an Instron 5543 mechanical tester using a 50 N load cell at a compression rate of 1 mm min⁻¹ and PBS bath set to 37 °C. Photo-lyogels were tested until 90% compression. The modulus extracted from the slope of the linear region of stress strain curve ranging from 0–40% strain.

Local Young's modulus of silk photo-lyogels ($n = 1$) hydrated in PBS, was measured using a JPK Nanowizard 4 Atomic Force Microscope (AFM) in force spectroscopy mode with a SNL-10-B probe (Bruker) which has a nominal spring constant of 0.12 N m⁻¹. The cantilever spring constant was determined by thermal tuning. Force curves were acquired by using an indentation force of 3 nN at indentation speed 2 μm s⁻¹. For each sample 5 areas of 1 μm² each were probed (>50 measurements per area). The Young's modulus was extracted from the slope of the force curve fitting a Hertz model.

2.6 Cell interactions with silk photo-lyogels

Silk photo-lyogels ($n = 5–6$) were hydrated in PBS, disinfected in 80% ethanol for 4 hours and incubated in Endothelial Cell Growth Medium-2 (EGM™-2) (Endothelial Cell Growth Medium-2 BulletKit™, Lonza, Australia) overnight at 4 °C. Photo-lyogels were blotted on a sterile tissue to remove excess liquid, and each seeded with 7.5×10^4 HUVECs (Lonza, Australia). Photo-lyogels were all seeded from a single direction and photo-lyogels without cells were used as controls. Photo-lyogels were placed in a 48-well plate and incubated at 37 °C with 5% CO_2 for 30 minutes before 10 μL of media was added to each sample. This addition of media was repeated three times and then 1 mL of media was added to each sample to fill the well.

After 24 or 72 h, photo-lyogels were removed from media, washed gently with PBS and cut along the middle, using a razor blade. Each photo-lyogel was incubated in 1 mL of 2 ng μL⁻¹ Calcein AM (Invitrogen) for 90 minutes at 37 °C with 5% CO_2. Samples were washed briefly in PBS and imaged using a Leica TCS SP2 Confocal Microscope, with excitation at 488 nm and emission at 505–540 nm. A z-stack of approximately 550 μm was created from a random area of the cross-section of the scaffold and averaged to create a single image. The mean intensity of the image was determined in ImageJ.

To analyze cell metabolic activity on the photo-lyogels an Alamar Blue assay was conducted. HUVECS were seeded onto photo-lyogels as before, but at a density of 5×10^4 cells per scaffold, with unseeded photo-lyogels used as controls. At multiple time points over an 11 day period, photo-lyogels were removed from media, washed gently with PBS, transferred to a fresh well plate and incubated with 400 μL of 10% Alamar Blue (Invitrogen) in full media at 37 °C with 5% CO_2 for 90 minutes. After incubation photo-lyogels were moved to a fresh 48-well plate with new media and the Alamar Blue solu-

tion was aliquoted into a non-binding 96-well black plate, read for fluorescence at excitation 540/35 and emission 600/40, using a Synergy™ HTX Multi-Mode Microplate Reader (BioTek Instruments, USA).

2.7 Tissue integration and vascularization of silk photo-lyogels

All procedures were conducted in accordance to animal ethics protocols approved by the UNSW animal ethics committee (ACEC 17/112B) on 8 weeks old female C57BL/6 mice. The back of each mouse was shaved and the surgical site disinfected 3× with betadine swabs followed by isopropanol wipes under general anesthesia of isoflurane. Analgesia was administered pre-operatively, with buprenorphine injected at 0.1 mg kg^{-1} subcutaneously. Silk photo-lyogels were implanted in a subcutaneous pockets on the back of each mouse (n = 6/condition; 3 scaffolds/mouse; scaffold location randomized). The incisions were closed with surgical clips that were removed at day 10 post-surgery. At week 4 post-surgery samples were explanted and processed for histological analyses.

Explanted samples were fixed in 10% buffered formalin at 4 °C for 24 h, incubated in 70% ethanol at 4 °C for 48 h and then embedded in paraffin. Samples were serially sectioned in a top-down plane to 5 μm thick (Leica RM2135 microtome) and stained with H&E as previously described.[30] Tissue infiltration in the middle of the photo-lyogel was quantified from H&E images using the Image J free-form section tool and comparing total area of tissue in a section to total photo-lyogel area.
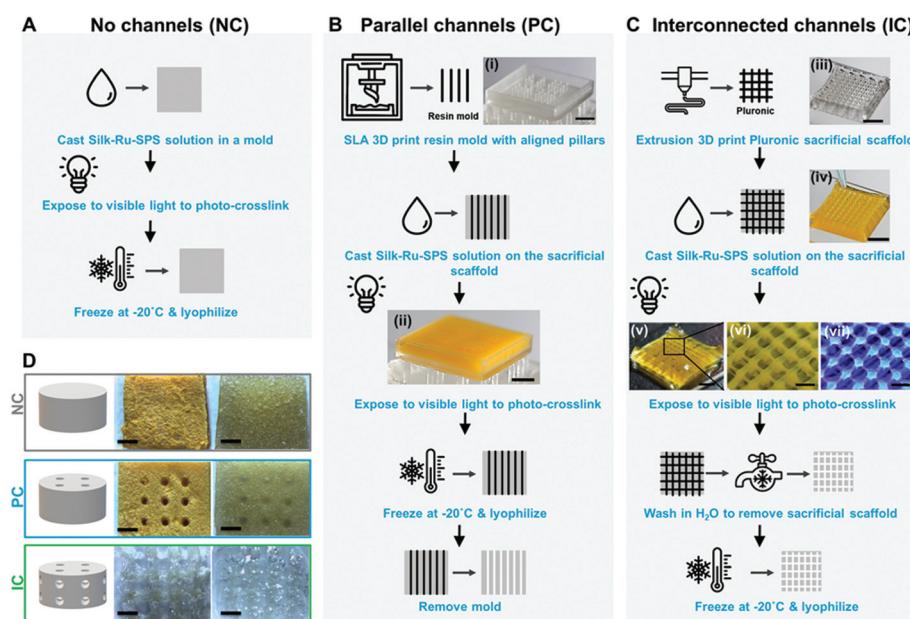
2.8 Statistical analyses

Statistically significant differences were determined by t-test, one- or two-way analysis of variance (ANOVA) and the Tukey post-test, or a non-parametric test (Kruskal–Wallis) where data was not normally distributed using GraphPad Prism. Data are expressed as mean ± standard deviation (SD) unless stated otherwise. Statistical significance was accepted at $p < 0.05$ and indicated in the figures as *$p < 0.05$, **$p < 0.01$, ***$p < 0.001$ and ****$p < 0.0001$.

3. Results and discussion

3.1 Fabrication of silk photo-lyogels containing microchannels

Silk photo-lyogels were fabricated with no microchannels (NC), an array of parallel microchannels (PC), or with interconnected microchannels (IC). Silk photo-lyogels without microchannels were fabricated by photo-crosslinking the silk solution followed by freezing at −20 °C and lyophilization (Fig. 1A). The resultant constructs were dry porous sponges with a yellow tint (as a result of the ruthenium color). Upon hydration, the constructs swelled, but were easy to handle and manipulate (Fig. 1D). Silk photo-lyogels with an array of vertical, parallel microchannels were fabricated in a similar manner to NC photo-lyogels, but the hydrogel was crosslinked around an SLA
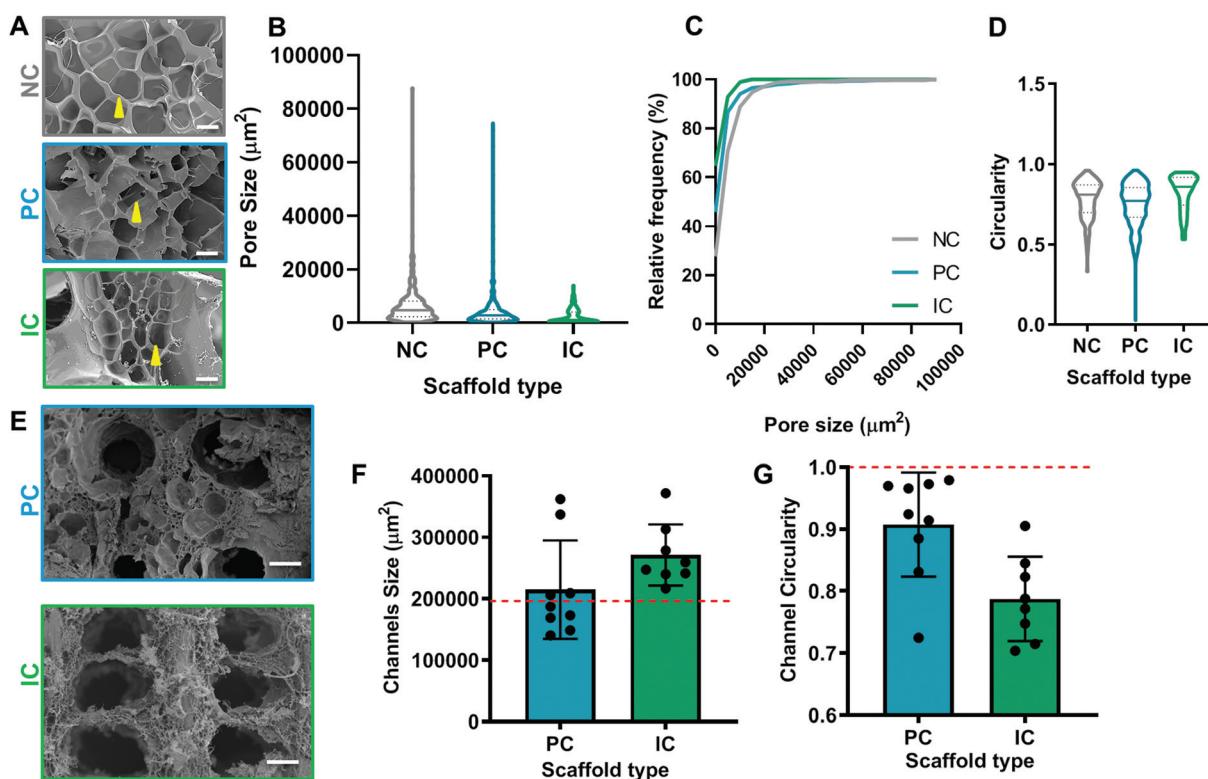
Fig. 1 Fabrication of silk photo-lyogels containing microchannels (A–C) schematic representation of the manufacturing approach, showing fabrication of silk photo-lyogels with (A) no microchannels (NC), (B) vertical, parallel microchannels (PC), and (C) interconnected horizontal and vertical microchannels (IC). Image (ii) shows a crosslinked silk hydrogel on the 3D printed mold. Image (iii) shows the extrusion printed sacrificial scaffold, while images (iv–vi) show the photo-crosslinked silk hydrogel cast around the sacrificial scaffold. Image (vii) shows silk fluorescence following UV irradiation, demonstrating formation of di-tyrosine bonds following photo-crosslinking. Scale bars are (i–v) 5 mm, (vi–vii) 500 μm. (D) Silk photo-lyogels with or without microchannels in their dry as-manufactured form and following hydration in PBS. Scale bars are 1 mm.

3D printed mold containing an array of 500 μm Ø pillars (Fig. 1B). The mold was removed following lyophilization, leaving behind an array of vertical microchannels (Fig. 1D). Silk photo-lyogels with interconnected microchannels were fabricated by crosslinking the silk solution around an extrusion 3D printed sacrificial template made of 500 μm Ø Pluronic strands arranged in a 0–90° pattern (Fig. 1C). The sacrificial template was removed in water following crosslinking, but prior to lyophilization, leaving behind an array of interconnected channels (Fig. 1D). Successful photo-crosslinking was demonstrated both by the stability of the constructs in aqueous environments, as well as silk fluorescence when irradiated under UV light showing typical di-tyrosine fluorescence[31] (Fig. 1C, vii).

Interestingly, while all photo-lyogels swelled considerably following hydration, IC photo-lyogels appeared to swell to a greater extent compared to the other two conditions (Fig. 1D). A combination of silk photo-crosslinking and 3D printing approaches therefore allowed a simple, accessible, and rapid means of fabricating microchannel with different morphologies into silk photo-lyogels. This combinatorial biomaterial fabrication approach allows generation of stable, dry constructs that can be stored at room temperature and used as off-the-shelf products in clinical applications.

3.2 Pore and channel morphology of silk photo-lyogels

The pore and channel morphology of silk photo-lyogels was assessed *via* scanning electron microscopy in dry state and confocal microscopy in hydrated state. The bulk of all silk photo-lyogels appeared porous with interconnected pores (Fig. 2A). The pore size was quantified as the area of the pore inlet and the median and average pore size were 4735 μm^2 and 6583 ± 424 μm^2 respectively for NC, 2812 μm^2 and 4751 ± 333 μm^2 for PC, and 1077 μm^2 and 2468 ± 199 μm^2 for IC photo-lyogels (Fig. 2B). While there was an overall trend toward smaller pores in IC photo-lyogels, and a small difference in the overall pore size distribution (Fig. 2C), the pore size difference was not significant between different conditions ($p > 0.05$). The pore inlets appeared roughly circular, with median and mean circularity ranging from 0.77 and 0.75 ± 0.005 respectively in PC to 0.86 and 0.82 ± 0.001 in IC photo-lyogels (Fig. 2D). Assuming circular pore inlets, the mean pore diameter was ~92 μm in NC, ~78 μm in PC, and ~56 μm in IC photo-lyogels. The average pore diameter of NC photo-lyogels was similar to that reported for lyophilized silk sponges made using 5–6% wt/v silk in uncrosslinked solution form.[32] All pore sizes were significantly higher than those in traditional hydrogels, which typically range from 5 to 100 nm.[33] The pores

Fig. 2 Pore and channel morphology of silk photo-lyogels. Pore and channel size were quantified from SEM images of photo-lyogels with no microchannels (NC), parallel microchannels (PC) and interconnected microchannels (IC). (A) SEM images of NC, PC and IC photo-lyogels showing pore morphology. Yellow arrows point to pores. Scale bars are 100 μm. (B–D) Quantification of the pore size and shape showing pore inlet area size (B), relative frequency of different pore sizes (C), and pore circularity (D). (E) SEM images of channel morphology in PC and IC photo-lyogels. Scale bars are 300 μm. (F and G) Quantification of the channel size (inlet area) and channel circularity. Red dashed line shows theoretical channel size and circularity.

were also larger than those of silk cryogels crosslinked using ethylene glycol diglycidyl ether (EDGE) crosslinker and N,N,N′, N′-tetramethylethylenediamine (TEMED) catalyst under similar freezing and silk concentration conditions.[34] It was interesting to note that the pore size distribution in IC samples appeared smaller even prior to swelling (Fig. 2), suggesting that the pore size difference is inherent to the process. This may be due to the crosslinking efficacy differences between different conditions, with the sacrificial scaffold in the IC condition affecting the crosslinking efficiency. This is supported by the higher swelling of the IC samples which would be expected in less densely crosslinked polymer networks. The lower crosslinking density would impact ice crystal formation as it affects the interactions between the growing ice crystals and crosslinked polymer mesh.[35,36] Aside from thermodynamics, ice templating operates on a foundation of displacement and entrapment.[37] In this setup, the crosslinked polymer mesh is displaced and pushed against the growing ice crystals. As observed with other ice-templated hydrogels, decreasing crosslinking density will decrease resistance of the mesh around the growing crystals and ultimately affect the size and morphology of the final pores.[35] A decrease in overall mesh resistance against the growing crystal limits its travel distance around the crystals, whereas the implied higher crosslinking density of the NC and PC samples could have accommodated higher resistance against and travel further along the growing crystals, resulting in larger pore sizes. It is important to note that this observed correlation is also dependent on the stiffness of the mesh itself. Stiffer and more viscous environments will impede ice crystal growth at an earlier point in the displacement phase and will result in smaller ice crystals, or even complete entrapment of the polymer, and therefore smaller pores.[38]
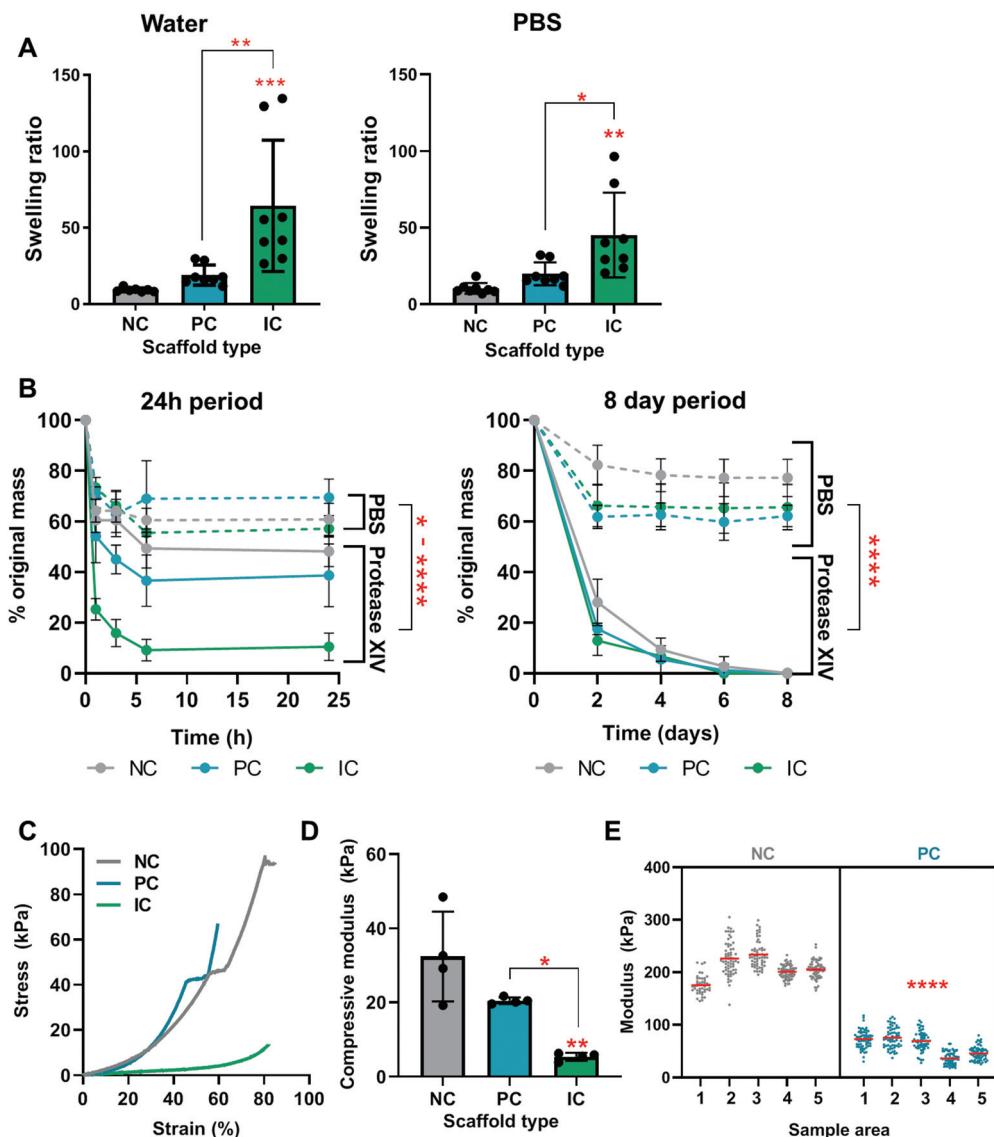
The theoretical channel diameter for both PC and IC scaffolds was 500 μm, translating to a theoretical channel inlet area of 196 350 μm² and circularity of 1. The channels in PC photo-lyogels showed a trend toward better adherence to expected theoretical channel morphology (Fig. 2E), with channel size of ~1.1-fold larger than theoretical, while IC photo-lyogels had channel size ~1.4-fold larger than theore-

tical (Fig. 2F). This increase in channel size in IC samples is likely due to differences in silk photo-lyogel hydration and the rate of sacrificial scaffold dissolution. Similarly, the PC channels were more circular, with circularity of 0.91 ± 0.08, while IC channels had lower circularity of 0.79 ± 0.07 (Fig. 2G). However, while these trends were observed, the differences in both channel cross sectional area and circularity were not significantly different between PC and IC photo-lyogels ($p > 0.05$). Better adherence to the original intended channel shape and size in PC photo-lyogels is likely a result of the more rigid mold made from the SLA printed plastic resin (for PC lyogels), relative to the softer, more malleable Pluronic sacrificial polymer (for IC lyogels). It has also been reported that SLA technologies allow structures with more defined resolution (50–100 μm voxel size) as compared to extrusion printing which often results in fibers of 150 μm.[39] While the SLA printed mold allowed better replication of the microchannel morphology, it does not allow easy generation of interconnected channels as a plastic mold with vertical and horizontal struts could not be easily remove from the silk lyogel. The sacrificial Pluronic scaffold on the other hand allows multiple channel configurations as it can be dissolved away from the silk lyogel by simple incubation in water.

Silk photo-lyogels were also imaged in their swelled state using confocal microscopy following staining with a fluorescent tracer. Due to the nature of this technique and the need to create optical sections through the sample, the pore and channel size were not quantified in their swelled state. However, based on qualitative observations (Fig. 3), it was obvious that silk photo-lyogels retained their porosity and open microchannels upon swelling. The pore size of NC and PC samples appeared similar to that in the dry state, while the pores in IC photo-lyogels appeared smaller than in their dry counterparts. The channels in PC photo-lyogels retained their circular geometry and original size, while the channels in IC photo-lyogels were open, but did deform from their initial intended circular geometry. This is consistent with the observations of higher IC photo-lyogel swelling observed visually in Fig. 1 and quantified in Fig. 4A.
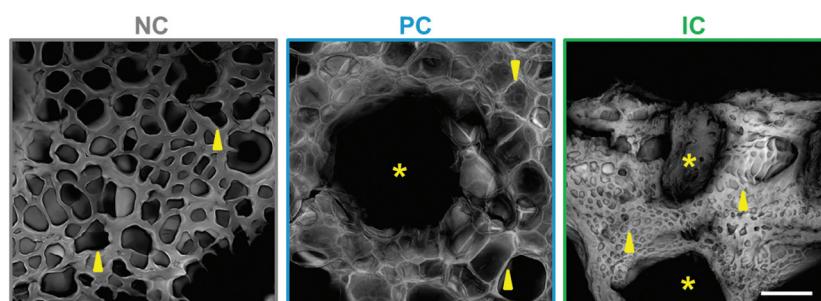
Fig. 3 Pore morphology in hydrated silk photo-lyogels. Pore morphology of photo-lyogels with no microchannels (NC), parallel microchannels (PC) and interconnected microchannels (IC) imaged in their hydrated (in PBS) form using confocal microscopy following TRITC staining. Images show average projections of 200 μm thick z-stacks. Scale bar is 200 μm. Yellow arrows point to representative pores, while asterisks show channels. GIFs showing pore morphology through the z-stack are available in ESI Fig. 1.†

Fig. 4 Physical properties of silk photo-lyogels. Silk photo-lyogels with no microchannels (NC), parallel microchannels (PC) and interconnected microchannels (IC) were assessed for their swelling, degradation and mechanical properties *in vitro*. (A) Photo-lyogel swelling in water and PBS showing mass change following hydration. Data are mean $\pm$ SD ($n = 8$). * ($p < 0.05$), ** ($p < 0.01$), *** ($p < 0.001$). (B) Photo-lyogel degradation in PBS and Protease XIV over a 24 h period and over an eight day period expressed as % of the original scaffold mass. Data are mean $\pm$ SD ($n = 3$ PBS, $n = 5$ Protease XIV). **** ($p < 0.0001$) showing overall difference between PBS and Protease XIV for all samples. Individual differences are not indicated on the graph for clarity, but are described in the Results section. (C and D) Mechanical properties of photo-lyogels following unconfined compression in hydrated (PBS) state, including representative stress–strain curves (C) and compressive modulus (D). Data are mean $\pm$ SD ($n = 4$). * $p < 0.05$, ** $p < 0.01$. (E) Mechanical properties of NC and PC photo-lyogels following nanoindentation with AFM, showing >50 measurements across five different areas of the scaffold. **** $p < 0.0001$ compared to NC. Data for IC samples could not be reliably obtained due to difficulties in immobilizing the sample.

The images in Fig. 3 show average projections of the z-stack obtained using confocal microscopy, which shows the overall morphology, but does not represent the pores in a single plane or the interconnected nature of the pores well. An animated view through the z-stack for each construct is therefore shown in Fig. S1.†

While some differences in pore size and microchannel integrity were observed between different fabrication techniques, both fabrication approaches allowed easy introduction of microchannels with different morphologies into 3D silk biomaterials and resulted in constructs that were easy to handle and manipulate which would be advantageous in clinical settings.

3.3 Physical properties of silk photo-lyogels

The swelling, degradation, and mechanical properties of silk photo-lyogels with different microchannel morphologies were quantified *in vitro*. All constructs increased in mass when

swelled in water or PBS and there was no significant difference in swelling in different solvents (water *vs.* PBS, $p > 0.05$). The swelling ratio of NC, PC, and IC photo-lyogels was 9.1 ± 1.3, 18.8 ± 6.6, and 64.3 ± 43.2 respectively when exposed to water, and 10.2 ± 3.5, 19.9 ± 7.5, and 45.2 ± 27.8 respectively when exposed to PBS (Fig. 4A). IC photo-lyogels swelled significantly more than their NC and PC counterparts, both in water and PBS ($p < 0.05$) (Fig. 4A). This increase in swelling is consistent with visual observations of IC photo-lyogels (Fig. 1) and observed changes in pore and channel morphology following swelling (Fig. 3). It is also consistent with a theoretical surface area increase in the presence of microchannels and inferred differences in crosslinking density. When we consider the overall surface area of PC and IC photo-lyogels (macroscopic, not considering pore surface area), the presence of microchannels increased the surface area of PC photo-lyogels 1.2-fold, and of IC photo-lyogels 1.7-fold compared to NC constructs, presumably allowing greater swelling. While there are few reports of silk lyogels in the literature, one study did compare the swelling ratios of silk lyogels formed *via* β-sheet induction at different silk concentrations. At the lowest concentration studied (3.2% wt/v) silk lyogels had a swelling ratio of 23.1, and the swelling ratio decreased with increasing silk concentration.[14] We observed a lower swelling ratio in 4% silk NC photo-lyogels, suggesting that the covalent crosslinking employed here reduced silk swelling. The swelling ratio of PC and IC scaffolds was on par and higher than those in the β-sheet-based lyogels, likely due to both increased surface area and decreased crosslinking density in the presence of channel molds. Fluid uptake and swelling are important parameters across a range of potential applications of these materials, as they will dictate the availability and density of absorbed biological molecules and mass transfer in tissue engineering applications, uptake and release kinetics of molecules in drug delivery applications,[14] and effective space filling in volumetric tissue injury replacement or in microfluidic devices.[40]

Silk photo-lyogel degradation was assessed in an accelerated *in vitro* degradation model using Protease XIV (Fig. 4B). While Protease XIV is a cocktail of bacterial proteolytic enzymes and does not represent silk degradation *in vivo*, it is a useful analytical tool extensively used to compare relative degradation rates of silk materials. We confirmed that lyophilization in the absence of crosslinking does not induce silk scaffold cross-linking and stabilization (Fig. S2†). Interestingly, unlike most silk constructs formed *via* β-sheet stabilization, di-tyrosine crosslinked silk photo-lyogels showed a degree of mass loss in PBS over the first 24 h of incubation, with most loss occurring within the first hour (Fig. 4B). Following this initial mass loss, the construct mass remained stable between ~60–80% of the original mass. This initial mass loss is likely attributed to loss of uncrosslinked silk protein, known as the soluble fraction. The soluble fraction for photo-crosslinked silk using the Ru/SPS was ~36%,[11] on par with that observed in this work. The mass loss in PBS was significantly higher in photo-lyogels containing microchannels compared to their NC counterpart ($p < 0.05$). This is likely due to the mold/sacrificial

scaffold affecting radical mobility during crosslinking, resulting in reduced crosslinking efficiency and density, as supported by swelling (Fig. 4A) and mechanical properties results (Fig. 4E). It is interesting to note though that the soluble fraction was not different in PC and IC lyogels when incubated in PBS (Fig. 4B), suggesting that while there may be a difference in crosslinking density that affected swelling and mechanical properties, it did not affect construct stability and soluble fraction loss. While silk photo-lyogels were stable in PBS after the initial soluble fraction loss, they degraded in Protease XIV, with almost complete mass loss by day 6. Significant differences between conditions were observed at the early time points (within the first 24 h) with IC samples degrading fastest, followed by PC and NC samples respectively (Fig. 4B). A significant difference in scaffold degradation between conditions was observed up to day 2, with significantly higher mass loss in PC ($p < 0.05$) and IC ($p < 0.0001$) photo-lyogels compared to NC photo-lyogels at day 2. No significant difference ($p > 0.05$) was observed between conditions at all subsequent time points. These early differences in scaffold degradation are likely a result of greater hydration and the hypothesized lower crosslinking density in IC samples.

Silk hydrogels crosslinked *via* hydrogen peroxidase initiated reaction rather than the photo-initiated reaction use here have previously been shown to be susceptible to Protease XIV degradation.[41] Crosslinking density correlates inversely with the degradation rate in silk and other polymer networks, likely due to smaller mesh size and more limited enzyme access.[41] Silk degradation is also known to be highly dependent on the material and protein structure, which dictates enzyme access to the cleavage sites.[42] For example, silk hydrogels were shown to degrade significantly faster and more than densely packed silk films,[42] and with lower β-sheet content.[7] Silk biomaterials also degrade *in vivo*, but little is currently known about the degradation rates of di-tyrosine crosslinked materials.

The presence of microchannels affected the bulk mechanical properties of silk photo-lyogels, with IC constructs having a significantly lower compressive modulus at 5.41 ± 1.10 kPa compared to that of NC at 32.42 ± 12.16 kPa ($p < 0.01$) and PC constructs at 20.49 ± 0.90 kPa ($p < 0.05$) (Fig. 4C and D). This effect is likely a result of both the void space created by microchannels allowing easier collapse of the structures, but also the likely difference in crosslinking density in IC constructs already discussed. The compressive modulus of NC constructs was lower than that of lyophilized silk sponges at the same concentration (~200 kPa, measured under tensile, rather than compression conditions).[8] However, it is difficult to directly compare mechanical properties between different studies as both the cross-linking and mechanical testing conditions often differ, resulting in drastic differences in reported mechanical properties. For example, compressive modulus of enzymatically crosslinked silk hydrogels has been reported at ~25 kPa (2% silk),[11] 0.3–1.5 kPa (3% silk) and 1–1.5 kPa (5% silk).[41,43] The local mechanical properties were measured *via* AFM nanoindentation and showed a significant decrease in the modulus of PC relative to NC samples (Fig. 4E). This is

further evidence for a decreased crosslinking density in PC relative to NC samples. Unfortunately the local mechanical properties of IC samples could not be reliably quantified as a result of difficulties in immobilizing the samples for measurement.

3.4 Cell interactions with silk photo-lyogels

Cell interactions with silk photo-lyogels were studied using HUVECs. HUVECs attached and proliferated on silk photo-lyogels over a 7 day period, showing a plateau between days 7 and 11 post-seeding by an Alamar Blue cell metabolic assay (Fig. 5A). While there was an overall trend for lower signal on NC photo-lyogels compared to PC and IC, there was no statistically significant difference observed between different conditions at any time point. Similarly, when the relative proliferation rate was described for each condition (signal relative to day 1), there was no difference between conditions (Fig. 5B),

suggesting silk photo-lyogels support cell proliferation to the same extent regardless of the presence of microchannels. Ruthenium/SPS cross-linked silk hydrogels have been shown to support cell encapsulation, supporting excellent cell viability, proliferation, and extracellular matrix deposition in human articular chondrocytes.[11] Similarly enzymatically cross-linked hydrogels (also *via* di-tyrosine bonds) were found to support cell adhesion and encapsulation.[9,44–48]

Even though the presence of microchannels did not affect the cell proliferation rate, it did improve the spatial distribution of cells throughout the 3D photo-lyogels, in particular on IC constructs (Fig. 5C and D). HUVECs were seeded on top of silk photo-lyogels, and at 24 h and 72 h post-seeding, scaffolds were sectioned along the midline, stained with calcein AM (live cells stained green) and imaged to assess cell distribution across the scaffold center. Visual observation and quantification of the fluorescence intensity showed a signifi-
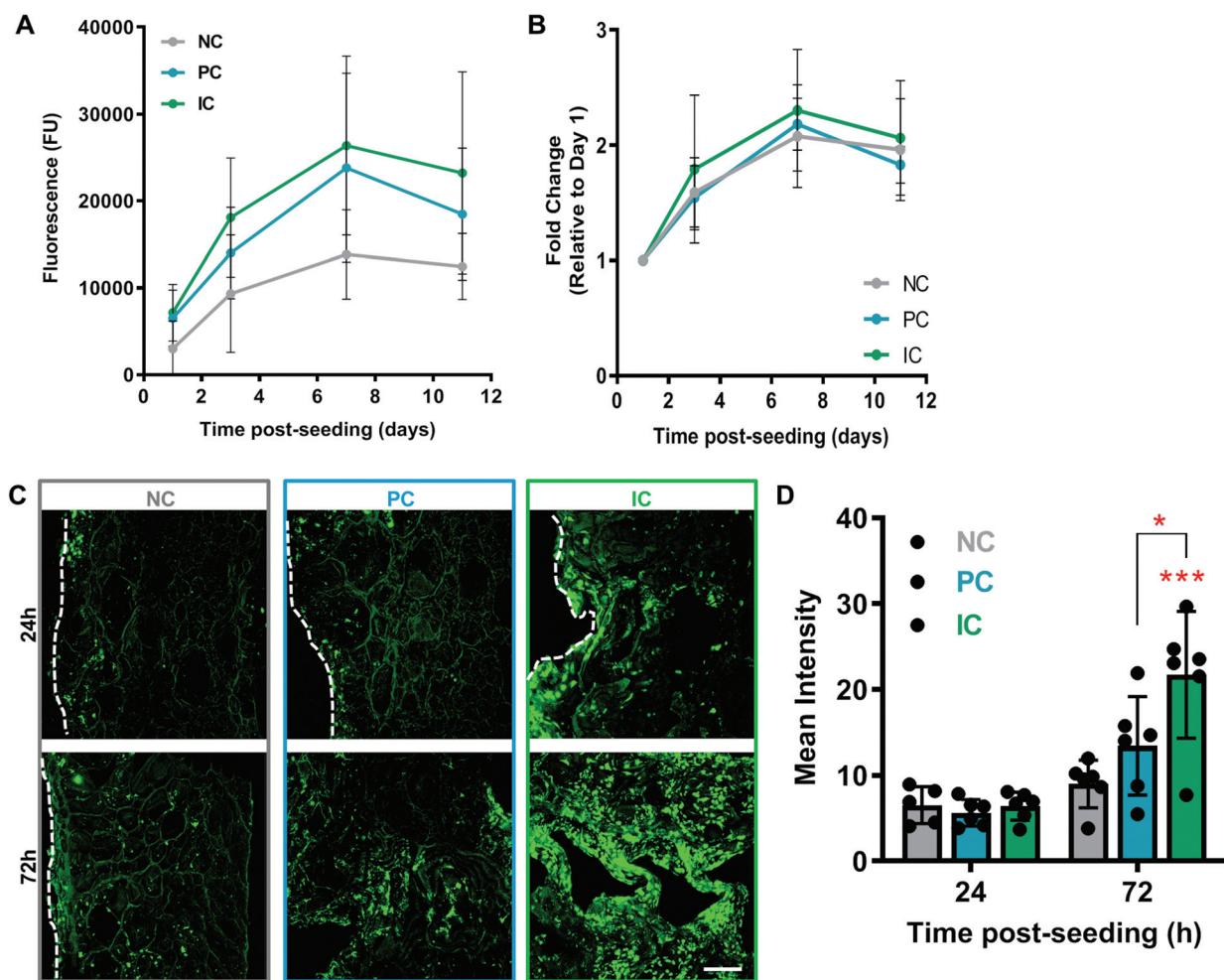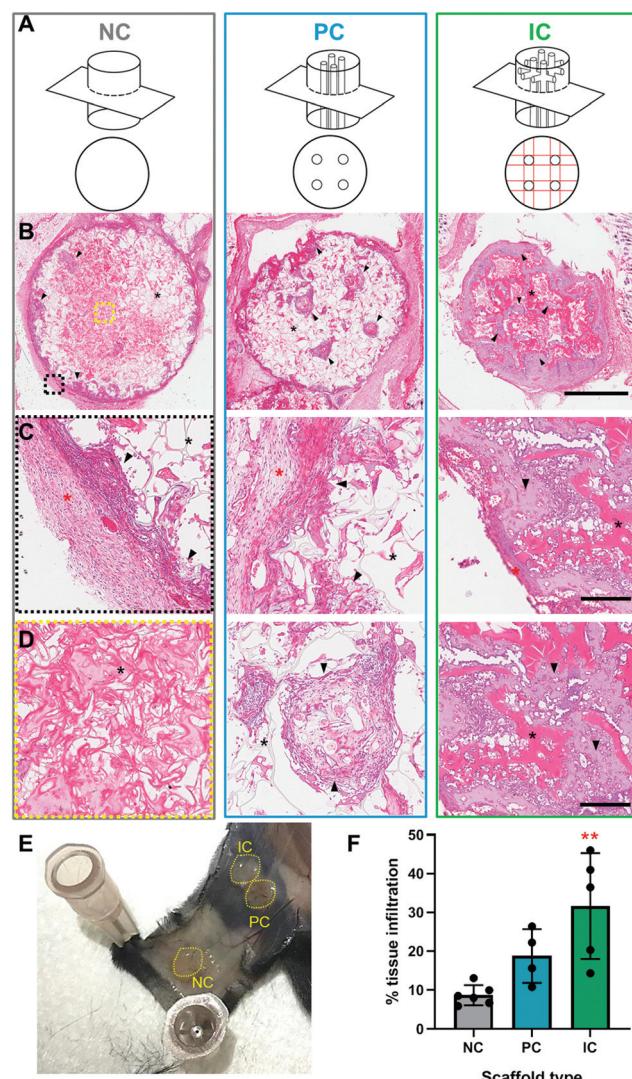

Fig. 5 Cell interactions with silk photo-lyogels. Silk photo-lyogels with no microchannels (NC), parallel microchannels (PC) and interconnected microchannels (IC) were seeded with endothelial cells and cell distribution and proliferation were assessed over time. (A and B) Endothelial cell proliferation on photo-lyogels over an 11 day period quantified using Alamar blue cell metabolic assay. Absolute fluorescence intensity is shown in (A), while relative cell proliferation (compared to day 1 for each condition) is shown in (B). Dashed lines show construct periphery. Data are mean ± SD (n = 5). (C and D) Calcein AM (live cells green) staining of endothelial cell distribution in the centre of photo-lyogels at 24 and 72 h post-seeding (A) and quantification of the fluorescence intensity from the confocal microscope images (B). Scale bar is 200 μm. Data are mean ± SD (n = 5–6), * (p < 0.05), *** (p < 0.001).

cant increase in cells at the center of scaffolds in IC photo-lyogels, compared to NC ($p < 0.001$) and PC ($p < 0.05$) constructs. It is likely that this difference is due to active cell migration through the scaffold in IC constructs, as similar cell distribution was observed between constructs at day 1 post-seeding (indicating it is not likely due to different seeding efficiencies and more homogenous initial seeding), and cells proliferated at similar rates in all the constructs (Fig. 5B), suggesting it is not a result of improved cell proliferation. This is an important feature toward *in situ* tissue engineering applications as active cell migration intro constructs is essential for tissue formation and remodeling. Di-tyrosine crosslinked hydrogels, on the other hand, have been shown to support cell encapsulation, but not active cell migration, making them more suitable for traditional rather than *in situ* tissue engineering approaches.[9] It is important to note that cell migration into the constructs is not the only requirement for *in situ* tissue engineering and it will be important to assess the potential of silk photo-lyogels for their regenerative potential in functional tissue injury models in future studies.

Patterning of endothelial cells has been shown to promote formation of functional vascular networks, compared to randomly oriented cells,[49–51] and confining endothelial cells within an aligned channel has been shown to result in cell signaling patterns beneficial for vascularization.[52] It is possible that microchannels in our scaffolds provided spatial cues for enhanced endothelial cell migration throughout large 3D biomaterials, which would provide an important cue for tissue vascularization in *in situ* tissue engineering using these biomaterials.

3.5 Silk photo-lyogel integration *in vivo*

Silk photo-lyogels were implanted in subcutaneous pockets in mice to assess the immune response to implants and their integration with the surrounding tissue. The photo-lyogels appeared well tolerated macroscopically, showing no irritation or swelling of implant pockets throughout the implantation period. Upon explantation, the constructs appeared well-integrated with the surrounding tissue, including a layer of fascia covering the constructs and were attached to the overlaying mouse skin (Fig. 6E). Explanted constructs were sectioned (perpendicular to the long axis of vertical channels) to observe different scaffold areas and channel morphology (Fig. 6A). All photo-lyogels showed a degree of fibrous encapsulation with layers of aligned fibroblasts and extracellular matrix surrounding the constructs (Fig. 6B–C). However, this did not prevent cell infiltration into the constructs, which was observed predominantly on the periphery of NC photo-lyogels, on the periphery and filling the channels of PC photo-lyogels and throughout the IC photo-lyogels (Fig. 6B & D). It was also interesting to note that the layer of fibrous encapsulation was much thinner in IC, compared to NC and PC photo-lyogels. The foreign body response to implanted constructs has been shown to be affected by a range of physical properties of the construct, including mechanical and morphological properties.[53] Additionally, studies have suggested optimal pore size for

Fig. 6 Silk photo-lyogel integration *in vivo*. Silk scaffolds with no microchannels (NC), parallel microchannels (PC) and interconnected microchannels (IC) were implanted subcutaneously in mice for 4 weeks. Explanted photo-lyogels and surrounding tissue were stained with H&E. (A) Schematic representation of photo-lyogel morphology and area represented in the H&E stained images in B–D. (B) Gross morphology of the middle of the photo-lyogels, showing the overall photo-lyogel shape and tissue infiltration. Scaffolds appear pink, while tissue appears purple. Black arrows point to representative areas of tissue infiltration, including construct periphery (all), through parallel microchannels (in PC photo-lyogels) and throughout photo-lyogels, between photo-lyogel struts in IC photo-lyogels. Black asterisk-silk photo-lyogel. Zoomed in images of photo-lyogel periphery (black box indicated in NC) and photo-lyogel centre (yellow box indicated In NC) for each condition are shown in panels C & D. (C and D) Magnified images showing different areas of the implanted photo-lyogels, including the scaffold periphery (C) and scaffold centre (D). Red asterisk-fibrous capsule, black arrows-tissue infiltration, black asterisk-photo-lyogel. Scale bars are 1 mm in (A) and 100 μm in C & D. (E) Gross appearance of the mouse skin during photo-lyogel explanation showing that the constructs were well integrated with the overlying skin and covered with a layer of fascia. (F) Tissue infiltration quantified from H&E stained images. Data are mean ± SD (n = 4–6), ** ($p < 0.01$) compared to NC photo-lyogels.

macrophage polarization toward the pro-healing M2 phenotype around 20–40 µm (ref. 54 and 55) which is in line with IC constructs.

Both visual observation and quantification of overall tissue ingrowth into the scaffolds showed an improvement in the presence of microchannels, with interconnected channels in IC photo-lyogels supporting a significant increase in tissue ingrowth into the construct compared to NC photo-lyogels ($p <$ 0.01) (Fig. 6F). This is in line with *in vitro* observations of improved endothelial cell migration on IC photo-lyogels. Interconnected microchannels are therefore a simple and accessible architectural feature that improves implanted silk photo-lyogel integration with the host tissue *in vivo*.

The cells infiltrating the scaffolds appeared predominantly fibroblastic, with elongated cell bodies and flattened nuclei, with obvious matrix deposition between the cells (Fig. 7A and B). Few foreign body giant cells were observed at week 4 post-implantation. The infiltrated tissue, in particular in IC photo-lyogels was well vascularized, with blood vessels with clear

lumen and perfused with red blood cells, indicating their functionality (Fig. 7A and B). The improved tissue and vascular ingrowth into IC photo-lyogels suggests the porosity and the presence of interconnected microchannels in these constructs are well-suited to tissue integration and thus *in situ* tissue engineering. Future studies will investigate the nature of the immune response to different constructs, including characterization of the macrophage phenotypes.

Silk degradation is difficult to assess and quantify *in vivo*, in particular in the current model due to sectioning challenges of IC scaffolds where it is not obvious if breaks in silk lamellae are due to sectioning or breakdown *in vivo*. However, it was interesting to note that the photo-lyogels appeared different morphologically in NC and PC compared to IC constructs. In NC and PC photo-lyogels, the silk lamellae appeared thin and fibrous when sectioned (Fig. 7C and D), similar to those of lyophilized silk sponges.[8] In IC photo-lyogels, silk lamellae appeared thicker and denser with a hydrogel-like morphology (Fig. 7E). All constructs had areas of intimate cell and tissue contact with the lamellae, but in IC photo-lyogels, there were areas where the cells appeared to have degraded lamellae strands, with tissue infiltration between photo-lyogel struts and areas of micro-cracks in the struts (Fig. 7E). This difference in construct morphology may be due to the previously described differences in crosslinking density and hydration state that were observed for IC photo-lyogels in this study (Fig. 3 and 4).

This first observation of di-tyrosine stabilized silk photo-lyogel interactions *in vivo* demonstrated that these constructs are relatively well tolerated *in vivo* showing a moderate immune response typical of silk biomaterials, and that the presence of microchannels, in particular interconnected microchannels, promotes improved tissue infiltration and integration *in vivo*. This suggests these constructs are promising implantable biomaterials for a range of tissue augmentation and regeneration applications and warrants further investigation into their performance in functional injury models.
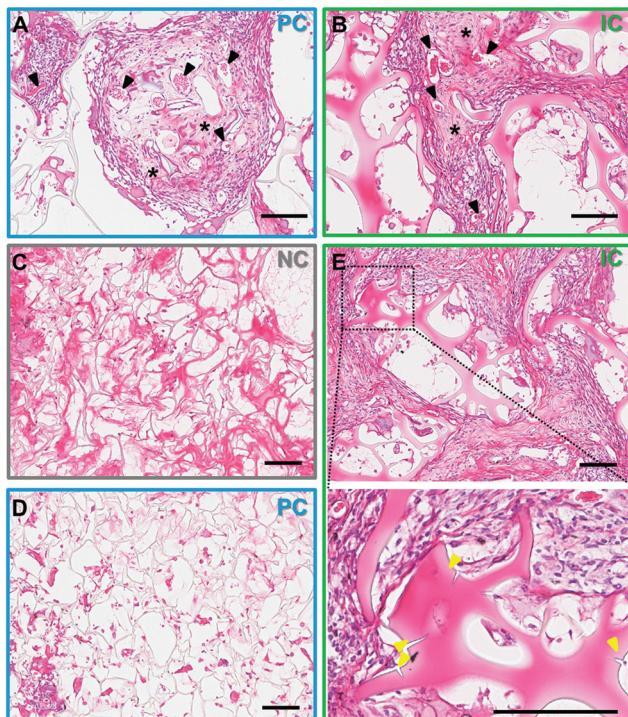
Fig. 7 Tissue and photo-lyogel morphology *in vivo*. Silk scaffolds with no microchannels (NC), parallel microchannels (PC) and interconnected microchannels (IC) were implanted subcutaneously in mice for 4 weeks. Photo-lyogels were stained with H&E. (A and B) Morphology of the tissue infiltrating into PC (A) and IC photo-lyogels (B) showing well-vascularized tissue with blood vessels showing well-defined lumens and perfused with red blood cells (black arrows), fibroblastic cells with elongated nuclei (purple staining) and extracellular matrix deposition (black asterisks). (C–E) Morphology of the silk photo-lyogels after 4 weeks, showing differences in morphology between NC/PC (C–D) and IC (E) constructs. The inset images in E shows areas of IC photo-lyogel breakdown, including large cracks between struts with tissue infiltrating through and micro-cracks (yellow arrows). Scale bars are 100 µm.

4. Conclusions

A combinatorial fabrication approach involving photo-initiated crosslinking of silk fibroin *via* di-tyrosine bonds followed by lyophilization resulted in 3D porous silk photo-lyogels with distinct physical properties and allowed an accessible and easy means of introducing parallel and interconnected arrays of microchannels into the photo-lyogel bulk. The presence of interconnected channels was shown to improve cell and tissue migration and photo-lyogel integration *in vivo*, making this a promising biomaterial format for *in situ* tissue engineering applications. Future studies will explore the utility of these biomaterials in functional injury models, as well as the biological mechanisms underpinning differences observed in IC constructs relative to their NC and PC counterparts in terms of cell migration and *in vivo* responses.

Conflicts of interest

There are no conflicts to declare.

Acknowledgements

References

1 T. B. Wissing, V. Bonito, C. V. C. Bouten and A. I. P. M. Smits, *NPJ Regener. Med.*, 2017, **2**, 18.

2 J. Fu and D.-A. Wang, *Trends Biotechnol.*, 2018, **36**, 834.

3 D. Sengupta, S. D. Waldman and S. Li, *Ann. Biomed. Eng.*, 2014, **42**, 1537.

4 K. S. Lim, M. Baptista, S. Moon, T. B. F. Woodfield and J. Rnjak-Kovacina, *Trends Biotechnol.*, 2019, **37**, 1189–1201.

5 C. Holland, K. Numata, J. Rnjak-Kovacina and F. P. Seib, *Adv. Healthcare Mater.*, 2019, **8**, 1800465.

6 D. N. Rockwood, R. C. Preda, T. Yucel, X. Q. Wang, M. L. Lovett and D. L. Kaplan, *Nat. Protoc.*, 2011, **6**, 1612.

7 X. Hu, K. Shmelev, L. Sun, E. S. Gil, S. H. Park, P. Cebe, *et al.*, *Biomacromolecules*, 2011, **12**, 1686.

8 J. Rnjak-Kovacina, L. S. Wray, K. A. Burke, T. Torregrosa, J. M. Golinski, W. W. Huang, *et al.*, *ACS Biomater. Sci. Eng.*, 2015, **1**, 260.

9 B. P. Partlow, C. W. Hanna, J. Rnjak-Kovacina, J. E. Moreau, M. B. Applegate, K. A. Burke, *et al.*, *Adv. Funct. Mater.*, 2014, **24**, 4615.

10 M. McGill, J. M. Coburn, B. P. Partlow, X. Mu and D. L. Kaplan, *Acta Biomater.*, 2019, **86**, 496.

11 X. Cui, B. Soliman, C. R. Alcala-Orozco, J. Li, M. A. M. Vis, M. Santos, *et al.*, *Adv. Healthcare Mater.*, 2020, 1901667.

12 B. P. Partlow, M. B. Applegate, F. G. Omenetto and D. L. Kaplan, *ACS Biomater. Sci. Eng.*, 2016, **2**, 2108.

13 K. J. De France, F. Xu and T. Hoare, *Adv. Healthcare Mater.*, 2018, **7**, 1700927.

14 N. Guziewicz, A. Best, B. Perez-Ramirez and D. L. Kaplan, *Biomaterials*, 2011, **32**, 2642.

15 B. K. Bhunia, D. L. Kaplan and B. B. Mandal, *Proc. Natl. Acad. Sci. U. S. A.*, 2018, **115**, 477.

16 B. Yetiskin and O. Okay, *Int. J. Biol. Macromol.*, 2019, **122**, 1279.

17 Y. Lu, S. P. Zhang, X. Y. Liu, S. F. Ye, X. Zhou, Q. L. Huang, *et al.*, *RSC Adv.*, 2017, **7**, 21740.

18 A. Zuluaga-Velez, D. F. Combita-Merchan, R. Buitrago-Sierra, J. F. Santa, E. Aguilar-Fernandez and J. C. Sepulveda-Arias, *PLoS One*, 2019, **14**(3), e0213303.

19 B. Yetiskin, C. Akinci and O. Okay, *Polymer*, 2017, **128**, 47.

20 E. Bellas, A. Rollins, J. E. Moreau, T. Lo, K. P. Quinn, N. Fourligas, *et al.*, *J. Biomed. Mater. Res., Part B*, 2015, **103**, 1217.

21 J. E. Brown, J. E. Moreau, A. M. Berman, H. J. McSherry, J. M. Coburn, D. F. Schmidt, *et al.*, *Adv. Healthcare Mater.*, 2017, **6**, 1600762.

22 J. Rnjak-Kovacina, L. S. Wray, K. A. Burke, T. Torregrosa, J. M. Golinski, W. W. Huang, *et al.*, *ACS Biomater. Sci. Eng.*, 2015, **1**, 260.

23 B. K. Bhunia, D. L. Kaplan and B. B. Mandal, *Proc. Natl. Acad. Sci. U. S. A.*, 2018, **115**, 477.

24 J. Rnjak-Kovacina, Y. W. Gerrand, L. S. Wray, B. Tan, H. Joukhdar, D. L. Kaplan, *et al.*, *Adv. Healthcare Mater.*, 2019, **8**, e1901106.

25 J. Rnjak-Kovacina, L. S. Wray, J. M. Golinski and D. L. Kaplan, *Adv. Funct. Mater.*, 2014, **24**, 2188.

26 W. L. Stoppel, D. Hu, I. J. Domian, D. L. Kaplan and L. D. Black, 3rd, *Biomed. Mater.*, 2015, **10**, 034105.

27 L. Tozzi, P.-A. Laurent, C. A. Di Buduo, X. Mu, A. Massaro, R. Bretherton, *et al.*, *Biomaterials*, 2018, **178**, 122.

28 A. H. Teuschl, J. Zipperle, C. Huber-Gries and D. L. Kaplan, *J. Biomed. Mater. Res., Part A*, 2017, **105**, 687.

29 K. Lerdchai, J. Kitsongsermthon, J. Ratanavaraporn, S. Kanokpanont and S. Damrongsakkul, *J. Pharm. Sci.*, 2016, **105**, 221.

30 F. Tang, X. D. Manz, A. Bongers, R. A. Odell, H. Joukhdar, J. M. Whitelock, *et al.*, *ACS Biomater. Sci. Eng.*, 2020, **6**, 1476–1486.

31 S. Mukherjee, E. A. Kapp, A. Lothian, A. M. Roberts, Y. V. Vasil'ev, B. A. Boughton, *et al.*, *Anal. Chem.*, 2017, **89**, 6136.

32 L. S. Wray, J. Rnjak-Kovacina, B. B. Mandal, D. F. Schmidt, E. S. Gil and D. L. Kaplan, *Biomaterials*, 2012, **33**, 9214.

33 N. Bhattarai, J. Gunn and M. Q. Zhang, *Adv. Drug Delivery Rev.*, 2010, **62**, 83.

34 F. Ak, Z. Oztoprak, I. Karakutuk and O. Okay, *Biomacromolecules*, 2013, **14**, 719.

35 M. Chau, K. J. De France, B. Kopera, V. R. Machado, S. Rosenfeldt, L. Reyes, *et al.*, *Chem. Mater.*, 2016, **28**, 3406.

36 X. Zhang, Y. Yu, Z. Jiang and H. Wang, *J. Wood Sci.*, 2015, **61**, 595.

37 K. L. Scotti and D. C. Dunand, *Prog. Mater. Sci.*, 2018, **94**, 243.

38 G. Shao, D. A. H. Hanaor, X. Shen and A. Gurlo, *Adv. Mater.*, 2020, 1907176.

39 K. S. Lim, J. H. Galarraga, X. Cui, G. C. J. Lindberg, J. A. Burdick and T. B. F. Woodfield, *Chem. Rev.*, 2020, **120**, 10662–10694.

40 A. Brown, H. He, E. Trumper, J. Valdez, P. Hammond and L. G. Griffith, *Biomaterials*, 2020, **243**, 119921.

41 O. Hasturk, K. E. Jordan, J. Choi and D. L. Kaplan, *Biomaterials*, 2019, **232**, 119720.

42 J. Brown, C. L. Lu, J. Coburn and D. L. Kaplan, *Acta Biomater.*, 2014, **11**, 212–221.

43 M. McGill, J. M. Coburn, B. P. Partlow, X. Mu and D. L. Kaplan, *Acta Biomater.*, 2017, **63**, 76.

44 W. Huang, A. Tarakanova, N. Dinjaski, Q. Wang, X. Xia, Y. Chen, *et al.*, *Adv. Funct. Mater.*, 2016, **26**, 4113.

45 T. Li, X. Song, C. Weng, X. Wang, J. Wu, L. Sun, *et al.*, *Int. J. Biol. Macromol.*, 2018, **115**, 300.

46 A. Sundarakrishnan, E. H. Acero, J. Coburn, K. Chwalek, B. Partlow and D. L. Kaplan, *Acta Biomater.*, 2016, **42**, 102.

47 X. Wang, Z. Ding, C. Wang, X. Chen, H. Xu, Q. Lu, *et al.*, *J. Mater. Chem. B*, 2018, **6**, 2739.

48 O. Hasturk, K. E. Jordan, J. Choi and D. L. Kaplan, *Biomaterials*, 2020, **232**, 19720.

49 J. D. Baranski, R. R. Chaturvedi, K. R. Stevens, J. Eyckmans, B. Carvalho, R. D. Solorzano, *et al.*, *Proc. Natl. Acad. Sci. U. S. A.*, 2013, **110**, 7586.

50 J. Rouwkema and A. Khademhosseini, *Trends Biotechnol.*, 2016, **34**, 733.

51 S. M. White, R. Hingorani, R. P. S. Arora, C. C. W. Hughes, S. C. George and B. Choi, *Tissue Eng., Part C*, 2012, **18**, 697.

52 J. H. Jeong, V. Chan, C. Cha, P. Zorlutuna, C. Dyck, K. J. Hsia, *et al.*, *Adv. Mater.*, 2012, **24**, 58.

53 J. I. Andorko and C. M. Jewell, *Bioeng. Transl. Med.*, 2017, **2**, 139.

54 L. R. Madden, D. J. Mortisen, E. M. Sussman, S. K. Dupras, J. A. Fugate, J. L. Cuy, *et al.*, *Proc. Natl. Acad. Sci. U. S. A.*, 2010, **107**, 15211.

55 E. M. Sussman, M. C. Halpin, J. Muster, R. T. Moon and B. D. Ratner, *Ann. Biomed. Eng.*, 2014, **42**, 1508.